Available online at www.sciencedirect.com
ScienceDirect
Journal of Power Sources xxx (2007) xxx–xxx
JOURNAL OF POWER SOURCES
www.elsevier.com/locate/jpowsour

$GdBaCo_2O_{5+x}$ layered perovskite as an intermediate temperature solid oxide fuel cell cathode

Albert Tarancón [a,*], Alejandro Morata [a], Guilhem Dezanneau [c], Stephen J. Skinner [b], John A. Kilner [b], Sònia Estradé [a], F. Hernández-Ramírez [a], F. Peiró [a], J.R. Morante [a]

[a] *EME/CeRMAE/IN² UB, Department of Electronics, University of Barcelona, Martí i Franquès 1, 08028 Barcelona, Spain*
[b] *Department of Materials, Imperial College London, London SW7 2AZ, United Kingdom*
[c] *Laboratoire SPMS, Ecole Centrale Paris (UMR CNRS 8580), Grande voie des vignes, 92295 Chatenay-Malabry Cedex, France*

Received 20 June 2007; received in revised form 20 August 2007; accepted 29 August 2007

Abstract

$GdBaCo_2O_{5+x}$ (GBCO) was evaluated as a cathode for intermediate-temperature solid oxide fuel cells. A porous layer of GBCO was deposited on an anode-supported fuel cell consisting of a 15 μm thick electrolyte of yttria-stabilized zirconia (YSZ) prepared by dense screen-printing and a Ni–YSZ cermet as an anode (Ni–YSZ/YSZ/GBCO). Values of power density of 150 mW cm^{-2} at 700 °C and ca. 250 mW cm^{-2} at 800 °C are reported for this standard configuration using 5% of H_2 in nitrogen as fuel. An intermediate porous layer of YSZ was introduced between the electrolyte and the cathode improving the performance of the cell. Values for power density of 300 mW cm^{-2} at 700 °C and ca. 500 mW cm^{-2} at 800 °C in this configuration were achieved.

Keywords: SOFC; GBCO; Cathode; Layered perovskite; Screen printing

1. Introduction

Lowering the operating temperature of solid oxide fuel cells (SOFCs) to the intermediate temperatures range (500–750 °C) in order to improve materials compatibility and reduce costs has become one of the main SOFC research goals [1,2]. However, decreasing the operating temperature means an increase of the resistive losses across the solid electrolyte and a similar magnification of the overpotentials at the air and fuel electrodes. Therefore, to preserve reasonable cell performance, this reduced-temperature regime should be achieved without compromising the internal resistance and the electrode kinetics of the cell.

Given the proven reliability of zirconia-based electrolytes in long-term SOFC tests [3], the use of yttria-stabilized zirconia (YSZ) electrolytes in reduced temperature fuel cells seems to be a logical choice although the intrinsic conductivity of the material becomes low at reduced temperatures. For conventional YSZ-supported SOFCs (150 μm thickness) the called for area-specific resistance (ASR) for SOFC applications (ASR = 0.15 Ω cm^2) requires operating temperatures over 1000 °C. However, the same ASR target can be achieved at temperatures as low as 700 °C using 15 μm thick YSZ layers [1]. Therefore, the use of YSZ for intermediate temperature applications requires the fabrication of anode- or cathode-supported SOFCs with electrolyte layers of few micrometers.

Albeit the ohmic losses across the electrolyte are clearly important, it is believed that the key to enhancing the power density of IT-SOFCs lies in the cathode performance. Due to the high activation energy, decreasing the operating temperature usually means that the cathode becomes the major source of electrical losses for the whole system [4]. Significant effort has been recently devoted to improve the poor catalytic activity of the traditional cathode materials and some excellent results have been achieved [5,6].

Many simple perovskite-type mixed ionic-electronic conductors such as doped $LaCoO_3$, $BaCoO_3$ or $LaFeO_3$ have been extensively studied as possible cathodes in SOFCs [1,5], however, not much attention has been paid to the perovskite related structures such as the double or layered perovskites.

* Corresponding author. Tel.: +34 934039159; fax: +34 934021148.
E-mail address: tarancon@el.ub.es (A. Tarancón).

0378-7753/$ – see front matter © 2007 Elsevier B.V. All rights reserved.
doi:10.1016/j.jpowsour.2007.08.077

Recent studies on layered cobaltites, i.e., $GdBaCo_2O_{5+x}$, $0 \leq x \leq 1$ (GBCO), by Maignan et al. [7] have shown that, in this structure, the Ba cations do not form a random distribution in the A perovskite sites but order in alternating (0 0 1) layers. Moreover, the oxygen vacancies, present when $0.45 < x < 0.6$, are mainly located in the rare earth planes $[GdO]_x$. This particular distribution seems to improve the oxygen transport properties compared to non-ordered perovskites [8]. According to these preliminary results, and considering an acceptable electronic conduction above the metal–insulator transition [7] ($T_{M-I} = 360$ K), GBCO appeared to be a suitable material for intermediate temperature (IT) SOFC cathode applications.

Recently the authors [9,10] have shown the potential of $GdBaCo_2O_{5+x}$ for cathode application in IT-SOFCs obtaining values for the ASR = 0.25 Ω cm^2 at 625 °C in symmetrical-cell systems. However, to our knowledge, the performance of GBCO cathodes as a part of a whole fuel cell has not been reported to date. This paper seeks to address this issue by evaluating the performance of this material working as a cathode in a standard anode-supported SOFC. In order to operate within the intermediate temperature range, while maintaining the excellent properties of YSZ, dense screen-printed layers of yttria-stabilized zirconia were deposited for the electrolyte [11,12].

The performance of the standard-configuration cell using a porous intermediate layer of YSZ between the electrolyte and the cathode was also evaluated.

2. Experimental

2.1. Inks and powder preparation and characterization

$GdBaCo_2O_{5+x}$ powder was prepared by the solid-state reaction of Gd_2O_3 (Johnson Matthey, 99.99%), $BaCO_3$ (Johnson Matthey, 99.9%) and Co_3O_4 (Ventro GMBH, 99.7%) dried powders. The mixture was successively calcined at 900 °C and 1000 °C in air for 20 h, with careful regrinding before each heat treatment until the single phase was obtained. The as-synthesized powders were ball milled in an organic vehicle (ethanol as a solvent and phosphate ester as a dispersant) for several days in order to prepare inks suitable for air brushing.

YSZ screen-printing ink samples were prepared as detailed elsewhere [12] by combining commercial 8 mol% Y_2O_3–ZrO_2 powder (MelChemicals) with an organic vehicle composed of terpineol as a solvent, phosphate ester as a dispersant, ethylcellulose as a binder and dibutyl phthalate as a plasticizer.

In order to structurally characterize the GBCO powders, X-ray diffraction patterns were collected at room temperature on a Siemens D500 diffractometer (Cu Kα source) in flat plate $\theta/2\theta$ geometry and selected area electron diffraction (SAED) was carried out in a transmission electron microscope (TEM) Phillips CM30 SuperTwin operating at 300 kV. High resolution TEM images of GBCO powder were obtained in a JEOL JEM 2010F TEM.

2.2. Single cell fabrication, characterization and testing

The optimized YSZ slurry was screen-printed (10 deposits) onto commercial NiO–YSZ tapes (ESL 42421, ESL Electroscience) of 180 micrometers thick used as an anode. The NiO–YSZ/YSZ half-cell was sintered at 1350 °C for 5 h under air. After the sintering stage, the GBCO ink was airbrushed onto the fully dense YSZ layer. A final heat treatment at 975 °C for 2 h in air was performed to achieve the best performance of the cathode. In order to have good current collection, platinum (Pt) nets were attached to the electrodes.

The electrical measurements were performed in a commercial gas tight double-chamber cell (ProboStat, NorEcs) placed inside a high temperature furnace (Fig. 1). To precisely determine experimental conditions, the temperature was obtained from a thermocouple located next to the sample. Gas mixtures were prepared by combining different gases by mass flow controllers. Flow rates between 50 ml min^{-1} and 200 ml min^{-1} were used. Two-probe galvanostatic measurements have been carried out using a Gamry Potentiostat PCI4/750. The electrochemical characterization was carried out using the same potentiostat working as an impedance analyzer. The frequency response was analyzed in the range of 100 mHz–300 kHz with an ac applied

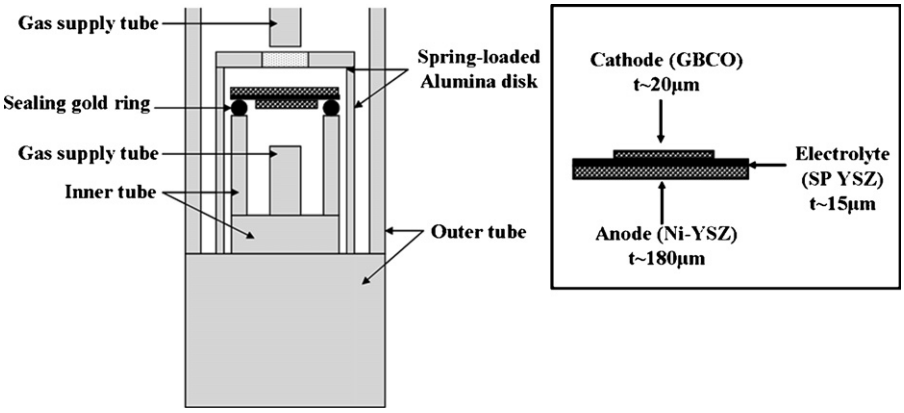

Fig. 1. Scheme of the ProboStat cell used for electrical characterization of the Ni–YSZ/YSZ/GBCO samples sketched in the box. Two independent chambers are allowed by sealing with a melted gold ring. Four leads (not drawn) contact the electrodes, connected pair wise for cell measurements and not interconnected for Van der Pauw measurements.

Please cite this article in press as: A. Tarancón, et al., J. Power Sources (2007), doi:10.1016/j.jpowsour.2007.08.077

signal of 50 mV. The LEVMW [13] complex non-linear square (CNLS) fitting program allowed us to interpret the measured impedance responses in terms of equivalent electrical circuits.

In-plane conduction measurements were performed using the Van der Pauw method [14] correcting for electrode and geometry effects. Four platinum contacts (A–D) placed on the surface of the layer were used to measure two different resistances, $R_{AB,CD} = V_{CD}/I_{AB}$ and $R_{BC,DA} = V_{DA}/I_{BC}$ (Keithley 2700 multimeter/7700 multiplexer module). If the measured sample thickness (t) is much less than its width and length, the following equation applies to the resistivity of the sheet (ρ):

$$\exp\left(-\frac{\pi R_{AB,CD}t}{\rho}\right) + \exp\left(-\frac{\pi R_{BC,DA}t}{\rho}\right) = 1 \quad (1)$$

Morphological characterization of the samples was carried out by scanning electron microscopy using a Leica Stereoscan S-360 equipment. Electron imaging in combination with the sputtering capability of a focused ion beam (FEI Dual beam DB232 [15]) was used to perform cross-section observations of the layered fuel cell devices.

3. Results and discussion

3.1. Powder characterization

The crystal structure adopted by $GdBaCo_2O_{5+x}$ has been reported to be dependent on the oxygen stoichiometry [7,16,17]. As previously reported, for $0.45 < x < 0.6$, the oxygen ions order into alternating filled and empty chains running along the a-axis, which results in the orthorhombic *Pmmm* and the doubling of the unit cell along the b-axis ($a_p x 2a_p x 2a_p$), here a_p refers to the basic cubic perovskite cell parameters (ca. 3.9 Å). This vacancy ordering is supposed to be the origin of the excellent oxygen transport properties.

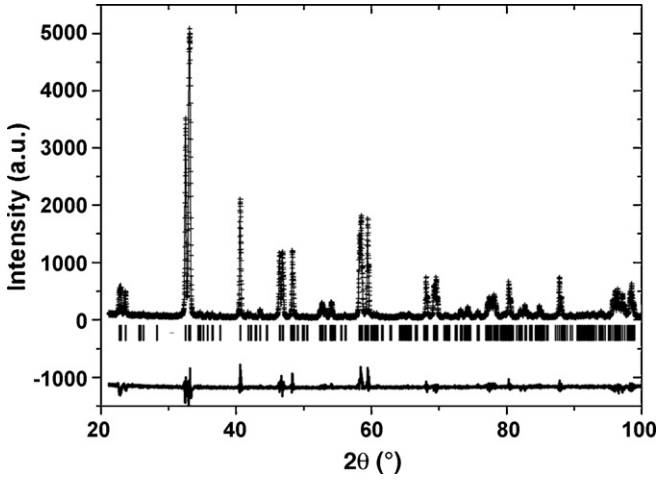

Fig. 2. Experimental (+), calculated and difference (solid lines) XRD pattern of $GdBaCo2O_{5+\delta}$-indexed to an orthorhombic *Pmmm* space group with unit cell: $a = 3.881(1)$ Å, $b = 7.840(2)$ Å, $c = 7.563(2)$ Å. The vertical bars show the Bragg angle positions corresponding to the structure. The Rietveld refinement presents reliability factors of $R_{Bragg} = 5.30$, $R_F = 4.11$, $R_p = 13.9$ and $R_{WP} = 15.5$.

Maignan et al. [7] reported different superstructures depending on the sintering atmosphere. For argon they obtained orthorhombic *Pmmm* with $a_p x a_p x 2a_p$ while for air they observed orthorhombic *Pmmm* with $a_p x 2a_p x 2a_p$. The samples for this work were synthesized in air so the $a_p x 2a_p x 2a_p$ unit cell is expected. As shown by the XRD pattern depicted in Fig. 2, the synthesized GBCO powder presents single-phase orthorhombic *Pmmm* symmetry with $a = 3.881(1)$, $b = 7.840(2)$, $c = 7.563(2)$ Å. The Rietveld refinement shows similar values for the atomic coordination (not presented here) reported in the literature by Frontera et al. [18].

To corroborate this result, electron diffraction and high-resolution-TEM imaging were carried out on the GBCO samples. Fig. 3(a) shows an electron diffraction pattern of a particle oriented in the [1 1 0] zone-axis. The cell doubling in c is due

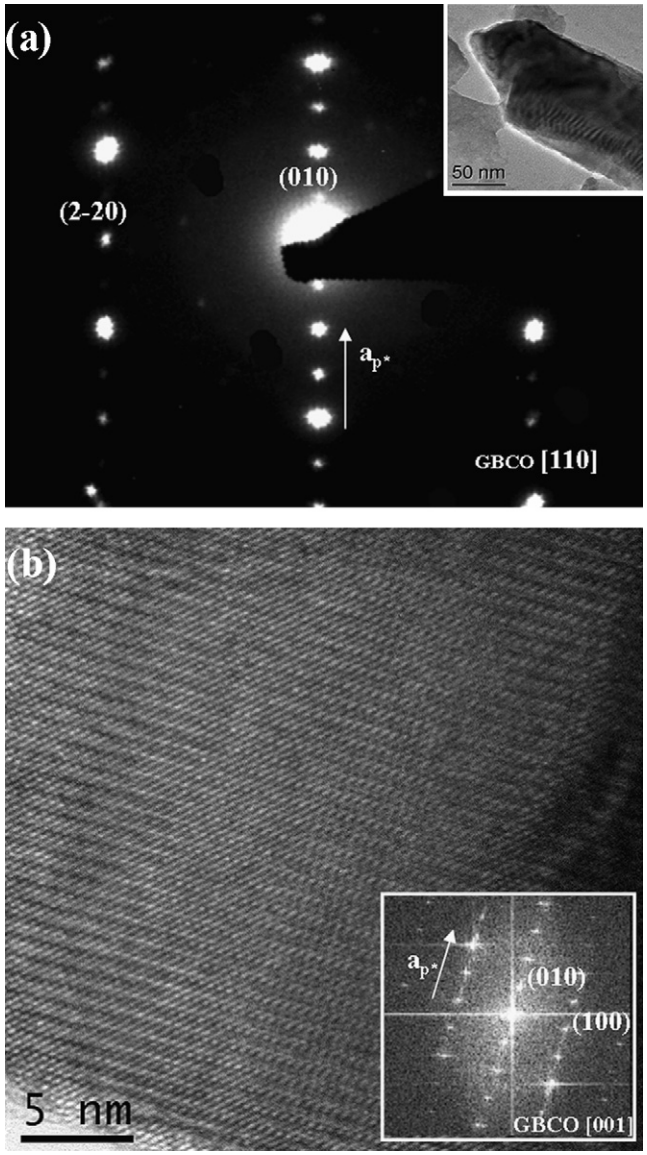

Fig. 3. (a) Electron diffraction pattern from a GBCO particle (shown in the inset). The cell doubling in c is due to ordering into layers of Gd and Ba perpendicular to z. (b) High-resolution image of a GBCO particle and corresponding FFT. The cell doubling in b is due to vacancy ordering in channels.

Please cite this article in press as: A. Tarancón, et al., J. Power Sources (2007), doi:10.1016/j.jpowsour.2007.08.077

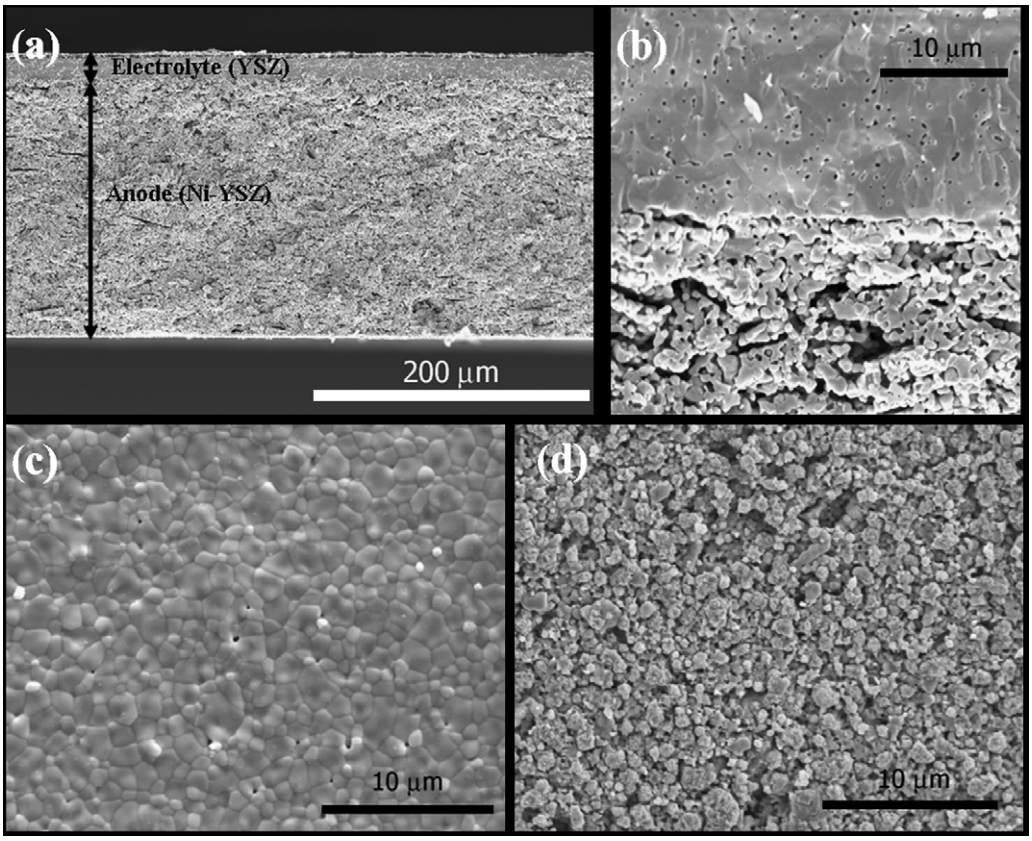

Fig. 4. (a) General view of a cross-section of a Ni–YSZ/YSZ half cell after reduction of the anode; (b) detail of the Ni–YSZ/YSZ interface; (c) surface view of the screen-printed YSZ layer; (d) surface view of the anode tape after reduction of NiO.

to doubling along the z direction. A high-resolution image of a GBCO particle and corresponding fast Fourier transform (FFT) are shown in Fig. 3(b). The figure shows the superstructure typical for air-synthesized materials, i.e., the vacancy ordering in channels that doubles the b parameter.

3.2. Morphological characterization

The YSZ layer screen-printed onto the Ni–YSZ anode (after reduction in 5%H_2/N_2 of the original NiO–YSZ) presents a high homogeneity of thickness (Fig. 4(a)). As previously reported by the authors [12], the average thickness of each deposited layer is ca. 1.5 μm and after 10 deposits a 15 μm thick electrolyte is obtained. The anode–electrolyte interface presents high connectivity as shown in Fig. 4(b). The thermal treatment used for sintering of the electrolyte allows achieving quasi full-density for the YSZ layer as observed in the SEM image depicted in Fig. 4(c). The grain size of the YSZ particles is around 2 μm. The anode layer also shows the required highly porous morphology, with average grain size ca. 500 nm, ensuring good gas diffusion (Fig. 4(d)).

The connection between the YSZ and the GBCO cathode is shown in Fig. 5(a) after cutting and polishing as carried out by a focused ion beam milling. The deposited layer shows a homogeneous aspect with grain sizes of ca. 500 nm (Fig. 5(b)). Partial delamination of the cathode layer is visible in other parts of the cell. It will be considered in detail in future sections.

3.3. Electronic conductivity of the electrodes

In order to verify good percolation and consequently good current collection, the anode and cathode in-plane conductivity of both anode and cathode were evaluated. Four point Van der Pauw measurements were carried out over a range of temperatures (T = 500–800 °C). Fig. 6 shows the dependence of the conductivity on temperature for the Ni–YSZ and GBCO layers calculated according to Eq. (1). Ni–YSZ layers present conductivity values around 10^2–10^3 S cm^{-1} in 5%H_2/N_2 as expected for the range of temperatures evaluated [19]. On the other hand, GBCO layers show conductivities of the order of a few tens of S cm^{-1} in air close to good electronic conductors such as $La_{0.8}Sr_{0.2}MnO_{3-\delta}$ ($\sigma \sim 100$ S cm^{-1} at 800 °C in air [20]). Therefore, cathode- and anode-electronic conductivities are high enough to ensure the flow of electrons from the current collector to the electron-consuming active sites.

3.4. Electrochemical and cell performance

Fig. 7 shows the impedance spectra (under open circuit conditions) of the anode-supported fuel cell using GBCO as the cathode and 5%H_2/N_2 as fuel over the temperature range 600–800 °C. There are two depressed arcs in every impedance spectroscopy curve, which reflects the electrode polarization resistances from both the anode and the cathode. At lower tem-

Please cite this article in press as: A. Tarancón, et al., J. Power Sources (2007), doi:10.1016/j.jpowsour.2007.08.077

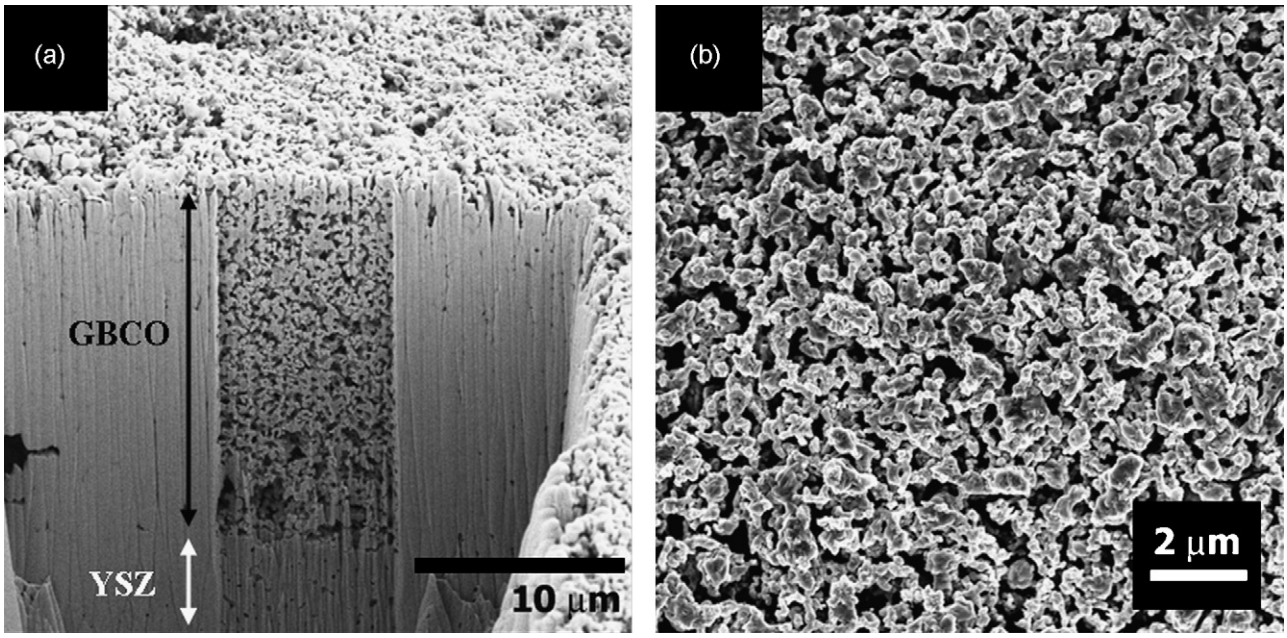

Fig. 5. (a) Electron image of the GBCO/YSZ interface cut using FIB (the image is tilted 52° so the distances have to be trigonometrically corrected); (b) planar view of the surface of the GBCO cathode. The cross-section present lateral effects because of higher ion currents used during FIB etching (500 pA for the rough etching and 50 pA for the fine central part).

peratures, the existence of an extra arc at lower frequencies is also observed. This small arc is usually associated to the gas diffusion limitation through the electrodes.

The electrochemical performance of the electrodes can be evaluated by splitting the characteristic impedance spectra for the whole cell into their main components. To deconvolute the obtained spectra, it is possible to use an equivalent circuit consisting of an inductance (L) in series with a resistance (R_{ohm}) in series with resistors attributable to the electrodes (R_{anode}, $R_{cathode}$) each of them in parallel with a constant phase element (Q_{anode}, $Q_{cathode}$), i.e., $LR(RQ)(RQ)$ as depicted in the inset of Fig. 8.

Albeit three-electrode impedance spectroscopy (with the reference electrode at the electrolyte) should be carried out in order to properly separate anode and cathode contribution, it seems reasonable to associate the arcs and the electrodes in the following way. The impedance of the anode is usually smaller at low current densities (compared to that of the cathode) becoming evident when increasing the current density (lowering the voltage) [21,22]. Fig. 8 shows the impedance spectrum for a whole cell at 650 °C under both open circuit voltage (Fig. 8a) and an applied voltage bias of 0.5 V (Fig. 8b). It is clear from the figure that when increasing the voltage the contribution of one of the arcs (low-frequency arc) becomes more pronounced. In the following

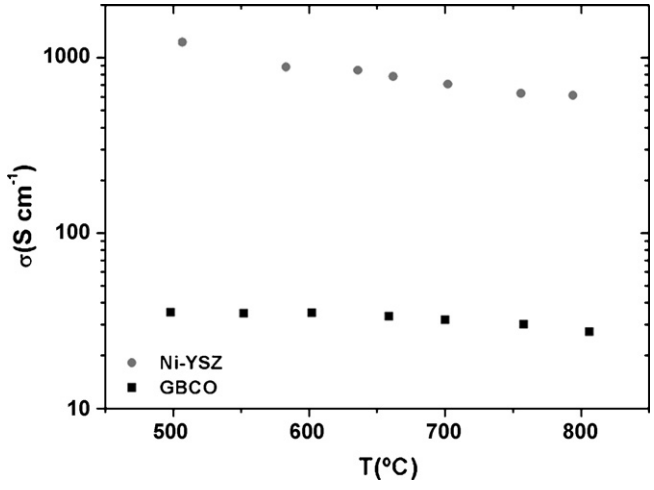

Fig. 6. In-plane conductivity as a function of temperature as evaluated by means of Van der Pauw measurements on a GBCO airbrushed layer ($t = 20$ μm) and Ni–YSZ tape ($t = 180$ μm).

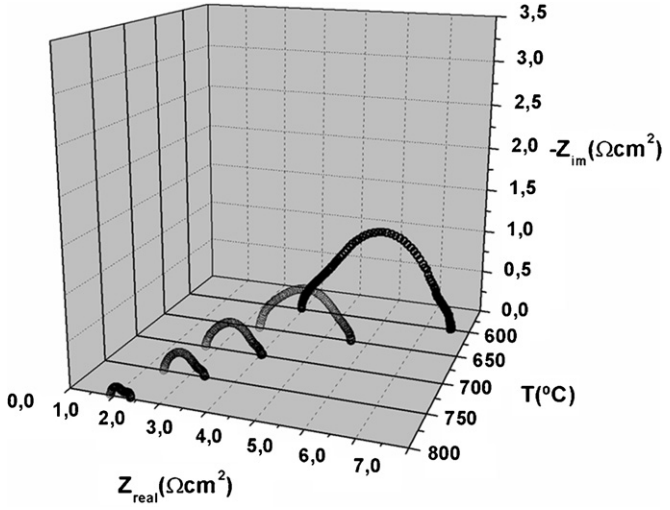

Fig. 7. Impedance spectra of the cell Ni–YSZ/YSZ/GBCO using 5%H_2/N_2 under open circuit conditions from 600 °C to 800 °C.

Please cite this article in press as: A. Tarancón, et al., J. Power Sources (2007), doi:10.1016/j.jpowsour.2007.08.077

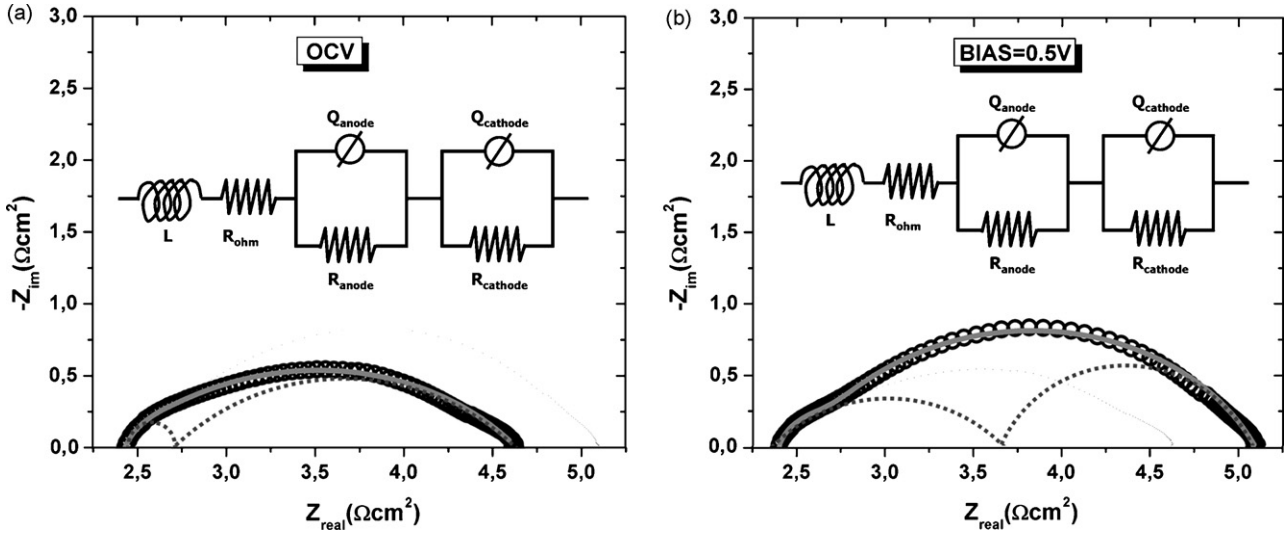

Fig. 8. Impedance spectra of the cell Ni–YSZ/YSZ/GBCO obtained at 650 °C under (a) open circuit voltage and (b) voltage bias of 0.5 V. Inset: equivalent circuit used for the deconvolution of the impedance spectra. The solid lines superimposed to the experimental data correspond to the fit and the dashed lines are guides for the eyes that show the high- and low-frequency arcs.

Table 1
Evolution with temperature of the different area-specific resistances of the cell under open circuit voltage conditions or with an applied voltage bias of 0.5 V

T (°C)	OCV			Bias = 0.5 V		
	R_{ohm} (Ω cm^2)	R_{anode} (Ω cm^2)	$R_{cathode}$ (Ω cm^2)	R_{ohm} (Ω cm^2)	R_{anode} (Ω cm^2)	$R_{cathode}$ (Ω cm^2)
602	2.45	1.29	2.77	2.34	2.24	2.52
654	1.89	0.42	2.04	1.80	1.43	1.69
705	1.19	0.34	1.17	1.08	0.89	1.04
756	0.89	0.16	0.92	0.74	0.47	0.83
807	0.51	0.09	0.40	0.28	0.20	0.43

analysis, this arc will be associated to the anode. Assuming this correspondence between arcs and electrodes, the values of the evolution of the cell resistance with the temperature[1] are listed in Table 1.

The anode/electrolyte interface shows an excellent performance with resistances below the target ASR of 0.25 Ω cm^2 in the intermediate range of temperatures (R_{anode} = 0.25 Ω cm^2 ca. 725 °C).

On the other hand, the ohmic contribution is too high. The ohmic contribution to the total resistance of the cell should correspond to the electrolyte ohmic loss. However, the estimated YSZ ohmic drop at 700 °C, considering a standard value of conductivity of σ = 0.01 S cm^{-1} and the average electrolyte thickness of our sample (15 μm), should not exceed values of 0.15 Ω cm^2 for the ASR (ASR = L/σ). Comparing this value with those listed in Table 1, it is obvious that the resistance arising from the oxide ionic motion through the electrolyte is not enough to explain the measured ohmic contribution. However, Fig. 9 shows for the ohmic resistance an Arrhenius type dependence on the temper-

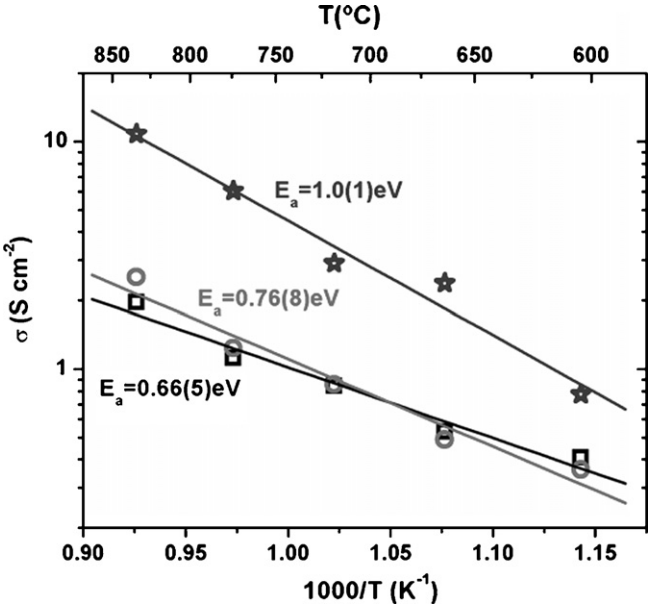

Fig. 9. Different contributions to the total conductivity of the cell as a function of the temperature: ohmic (squares), anode interfacial (stars) and cathode interfacial (circles). In all the cases, the conductivities represented correspond to open circuit voltage conditions.

[1] The so-called *ohmic* resistance has been corrected by removing the resistance in series corresponding to the wires. A calibration of this background resistance has been carried out by short-circuiting the measurement cell at different temperatures.

Please cite this article in press as: A. Tarancón, et al., J. Power Sources (2007), doi:10.1016/j.jpowsour.2007.08.077

ature with an activation energy of $E_a = 0.66(5)$ eV, close to that for the ionic conductivity of the yttria-stabilized zirconia. Therefore, an increase of the resistance due to geometrical aspects is proposed. A reduction of the area of the contact region of the electrolyte–electrode interface would result in an increase of the estimated ASR ($ASR = R_{observed} \times S$, where S is the area) without changing the temperature dependence.

Different possibilities can be argued to explain the origin of a hypothetical reduction of the active contact area. For instance, the formation of insulating phases in the electrolyte/cathode interface has been extensively reported for lanthanum containing cathodes on YSZ electrolytes [23]. The formation of the insulating lanthanum zirconate phase ($La_2Zr_2O_7$) represents one of the most relevant drawbacks for the state-of-the-art cathodes of the stabilized zirconia system. For our cathode, an equivalent lanthanide zirconate pyrochlore could be expected, i.e., $Gd_2Zr_2O_7$. Although the pyrochlore structure is stable in the Gd–Zr–O system for our range of temperatures [24], other work has not shown the formation of the gadolinium zirconate pyrochlore, e.g., Takeda et al. [25] do not observe it between 8YSZ and $Gd_{0.8}Sr_{0.2}MnO_{3-\delta}$ at 1000–1400 °C. Actually, the gadolinium zirconate pyrochlore has the narrowest region of existence among the lanthanide zirconate pyrochlores. The enthalpy of formation of $Ln_2Zr_20_7$ (Ln = Lanthanides) decreases with decreasing ionic radius of the rare earth cation [26] and therefore, the stability of the pyrochlore is reduced in the order $La_2Zr_2O_7 > Pr_2Zr_2O_7 > Nd_2Zr_2O_7 > Gd_2Zr_2O_7$ [27].

Another cause of active area reduction is having inadequate connectivity of the cathode and electrolyte layers. As shown in Fig. 10, a few gaps due to partial delamination of the cathode layer have been observed for our cells. This delamination is probably due to either the low roughness of the electrolyte layer, which would make cathode attachment difficult, or the different thermal expansion coefficients between yttria-stabilized zirconia (TEC $\sim 10 \times 10^{-6}\,K^{-1}$) and cobaltites (e.g., TEC $\sim 22 \times 10^{-6}\,K^{-1}$ for $LaCoO_3$). Apart from increasing the ohmic contribution to the total resistance, this partial detachment would increase the area-specific resistance associated to the cathode/electrolyte interface due to the reduction of the active area. As previously mentioned and shown in Fig. 9, this cathode/electrolyte interface represents the other main contribution to the final impedance.

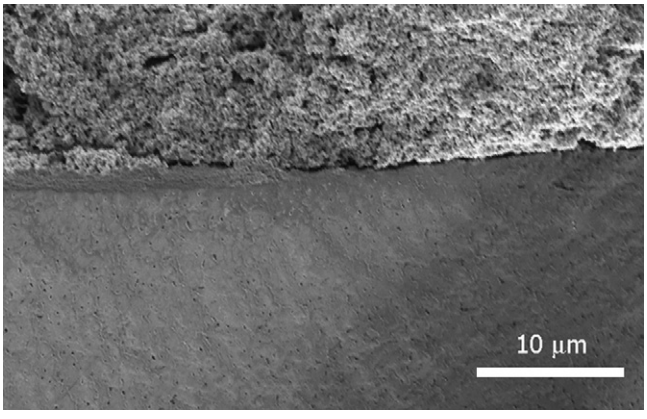

Fig. 10. SEM image of the YSZ/GBCO interface presenting partial delamination of the cathode layer (on the top face).

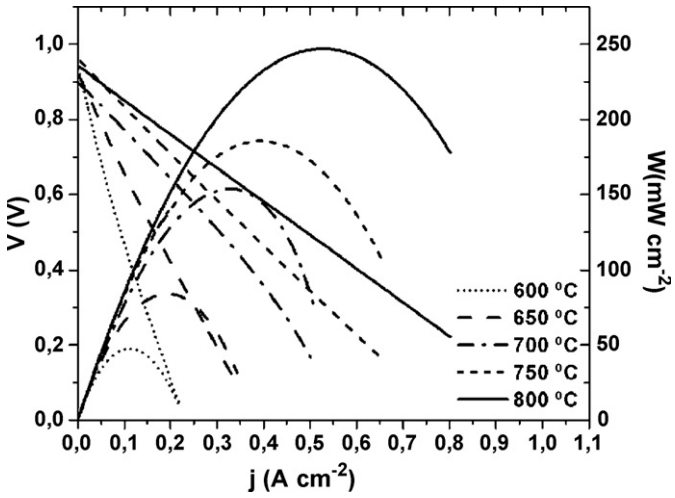

Fig. 11. Power density and voltage as a function of current density for a cell Ni–YSZ/YSZ/GBCO under 5%H_2/N_2 as fuel and air as oxidant in the temperature range from 600 °C to 800 °C.

3.5. Power density of the cell

Fig. 11 shows the variation of cell voltage and power density as a function of current density for the Ni–YSZ/YSZ/GBCO cell under 5%H_2/N_2 from 600 °C to 800 °C. Small deviations from the expected dependence of the OCV with temperature, i.e., OCV increase by temperature decrease, suggest some instability in the electrode performance with temperature and flow rate.

As shown in Fig. 11, galvanostatic single cell tests yielded open circuit voltages (V_{OC}) of $V_{OC} = 950$ mV at 800 °C. The theoretical value for the open circuit voltage at this temperature is $V_{OC} = 1.1$ V and the value reported from gas permeability measurements for thin YSZ electrolytes [28] with permeabilities on the order of 10^{-18} m^2 is $V_{OC} = 1.05$ at 850 °C (these values were obtained for pure H_2). These results indicate that good print conditions and inks for the YSZ layer fabrication method were achieved.

The power density of the cell increases with increasing the operating temperature. Maximum power densities of the cell are 250 mW cm^{-2} and 150 mW cm^{-2} at 800 °C and 700 °C, respectively.

3.6. Intermediate YSZ layer to improve electrolyte–cathode interface

The previously mentioned ohmic and electrolyte–cathode interfacial impedance constitute the main contribution to the total impedance of the cell. According to our results, the most likely explanation for this behaviour is an inadequate connectivity between the cathode and electrolyte layers. An insufficient connectivity between electrolyte and cathode leads to a reduction of the real active surface involved in the electrochemical processes. In order to overcome this major drawback, an increase of the roughness of the electrolyte is proposed to

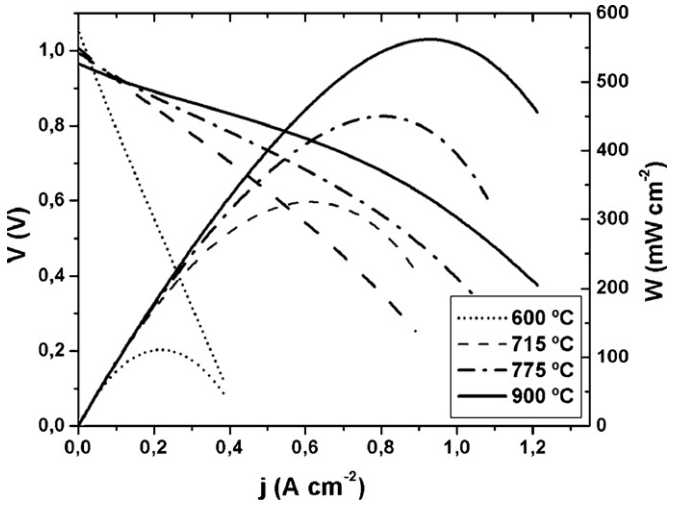

Fig. 12. Power density and voltage as a function of current density for a cell Ni–YSZ/YSZ/GBCO under 5%H_2/N_2 as fuel and air as oxidant in the temperature range from 600 °C to 900 °C. In order to improve the electrolyte–cathode interface, an intermediate layer of YSZ has been airbrushed and sintered at 1200 °C.

improve the connectivity between the electrolyte and cathode layers. An intermediate layer of YSZ was airbrushed onto the NiO–YSZ/YSZ sintered half-cell. A low sintering temperature was used to attach this layer (1200 °C for 3 h) to obtain a porous structure. This new layer should be applied taking into account that a balance between roughness and thickness of the electrolyte has to be kept.

Preliminary results obtained for these improved cells are very promising. Fig. 12 shows the power density as a function of current density. The non-linearity of these curves is due to the dominant electrode polarization effect (compare to the linearity observed in Fig. 11 where the ohmic was the main contribution). Maximum power densities of the cell are 550 mW cm^{-2} and 300 mW cm^{-2} at 900 °C and 700 °C, respectively. The maximum power density at 800 °C is close to the often-considered target value of 500 mW cm^{-2} for technological applications.

These results demonstrate that GBCO-based solid oxide fuel cells may render high performances in the intermediate temperature regime. In addition, the performance reported here could be significantly improved by using humidified pure H_2 as the fuel and oxygen as the oxidant instead of dry 5%H_2/N_2 and air. An increase in performance of two and even three times has been reported for other materials when changing from 5%H_2 to pure H_2 atmospheres [29,30]. Many authors have reported the benefits of increasing the water content for fuel cell performance [31].

4. Conclusions

Anode-supported solid oxide fuel cells based on an 8 mol% Y_2O_3–ZrO_2 electrolyte and a $GdBaCo_2O_{5+x}$ cathode were fabricated and evaluated. The YSZ layer was deposited by a dense screen-printing technique achieving a thickness of 15 μm with a quasi-full density at sintering temperatures as low as 1350 °C. Both anode and cathode electrodes showed a high homogeneity with a narrow distribution of grain sizes around 500 nm. The figures of performance of this standard fuel cell with a GBCO cathode are high, with power densities ca. 250 mW cm^{-2} at 800 °C and 150 mW cm^{-2} at 700 °C. However, better values were expected according to results obtained for each individual component. Poor electronic conductivity of the electrodes was rejected after in-plane conductivity evaluation by Van der Pauw measurements. Complete deconvolution of impedance spectra at different temperatures enabled the major contributions to the total impedance to be analyzed. An inadequate connectivity between the electrolyte and cathode layers is considered to be the origin of this excess of impedance. In order to address this issue, an intermediate porous layer of YSZ was deposited between the electrolyte and the cathode. The performance of this new cell is considerably improved over the previous version. The cell achieved values of power density close to the target value of 500 mW cm^{-2} at temperatures below 800 °C. These results indicate that the SOFC system presented here (5%H_2/N_2, Ni–YSZ/YSZ (screen-printed)/YSZ (airbrushed)/GBCO, Air) represents an excellent candidate for intermediate temperature applications. Moreover, a significant enhancement of the performance of the cell is expected by optimizing the fuel composition.

Acknowledgement

This work was supported by the Generalitat de Catalunya (CeRMAE).

References

[1] N.P. Brandon, S. Skinner, B.C.H. Steele, Annu. Rev. Mater. Res. 33 (2003) 183.
[2] B.C.H. Steele, A. Heinzel, Nature 414 (2001) 345.
[3] L. Blum, W.A. Meulenberg, H. Nabielek, R. Steinberger-Wilckens, Int. J. Appl. Ceram. Technol. 2 (2005) 482.
[4] J. Fleig, Annu. Rev. Mater. Res. 33 (2003) 361.
[5] S.J. Skinner, Int. J. Inorg. Mater. 3 (2001) 113.
[6] Z. Shao, S.M. Haile, J. Ahn, P.D. Ronney, Z. Zhan, S.A. Barnett, Nature 435 (2005) 3676.
[7] A. Maignan, C. Martin, D. Pelloquin, N. Nguyen, B. Raveau, J. Solid State Chem. 142 (1999) 247.
[8] A.A. Taskin, A.N. Lavrov, Y. Ando, Appl. Phys. Lett. 86 (2005) 91910.
[9] A. Chang, S.J. Skinner, J.A. Kilner, Solid State Ionics 177 (2006) 2009.
[10] A. Tarancón, S.J. Skinner, R.J. Chater, F. Hernández-Ramírez, J.A. Kilner, J. Mater. Chem. 17 (2007) 3175.
[11] A. Tarancón, G. Dezanneau, J. Arbiol, F. Peiró, J.R. Morante, J. Power Sources 118 (2003) 256.
[12] A. Morata, A. Tarancón, G. Dezanneau, F. Peiró, J.R. Morante, Nanostructured Materials in Alternative Energy Devices, in: E.M. Kelder, E.R. Leite, J.-M. Tarascon, Y.-M. Chiang (Eds.), Mater. Res. Soc. Symp. Proc. 822, S6.11, Warrendale, PA, 2004.
[13] J.R. Macdonald, L.D. Potter Jr., Solid State Ionics 23 (1987) 61;
J.R. Macdonald, J. Comput. Phys. 157 (2000) 280;
The newest Windows version, LEVMW, of the comprehensive LEVM fitting and inversion program may be downloaded at no cost from http://www.physics.unc.edu/~macd/. It includes an extensive manual and executable and full source code. More information about LEVM is provided at this www address.
[14] L.J. Van der Pauw, Philips Res. Rep. 13 (1958) 1.
[15] Strata DB. 235 Product data sheet, FEI Company.
[16] J.C. Burley, J.F. Mitchell, S. Short, D. Miller, Y. Tang, J. Solid State Chem. 170 (2003) 339.

[17] Y. Morimoto, T. Akimoto, M. Takeo, A. Machida, E. Nishibori, M. Takata, M. Sakata, K. Ohoyama, A. Nakamura, Phys. Rev. B 61 (2000) R13325.
[18] C. Frontera, J.L. García-Muñoz, A. Llobet, M.A.G. Aranda, Phys. Rev. B 65 (2002) 180405.
[19] D. Simwonis, F. Tietz, D. Stöver, Solid State Ionics 132 (2000) 241.
[20] E.O. Ahlgren, F.W. Poulsen, Solid State Ionics 86–88 (1996) 1173.
[21] Fuel Cell Handbook (7th ed.) by E.G. & G. Services for the US Department of Energy, National Technical Information Service, Springfield, VA, 2004.
[22] S. Souza, S.J. Visco, L.C. de Jonghe, Solid State Ionics 98 (1997) 57.
[23] D. Kuscer, J. Holc, M. Hrovat, S. Bernik, Z. Samardzija, D. Kolar, Solid State Ionics 78 (1995) 79.
[24] S. Lakiza, O. Fabrichnaya, Ch. Wang, M. Zinkevich, F. Aldinger, J. Eur. Ceram. Soc. 26 (2006) 233.
[25] Y. Takeda, H.Y. Tu, H. Sakaki, S. Watanabe, N. Imanishi, O. Yamamoto, M.B. Phillipps, N.M. Sammes, J. Electrochem. Soc. 144 (1997) 2810.
[26] M. Bolech, E.H.P. Cordfunke, A.C.G. van Genderen, R.R. van der Laan, F.J.J.G. Janssen, J.C. van Miltenburg, J. Phys. Chem. Solids 58 (1997) 433.
[27] G. Ch. Kostogloudis, Ch. Ftikos, J. Eur. Ceram. Soc. 18 (1998) 1707.
[28] C.J. Li, C.X. Li, M.J. Ning, Vacuum 73 (2004) 699.
[29] J.C. Ruiz-Morales, J. Canales-Vázquez, J. Peña-Martínez, D. Marrero-López, P. Núñez, Electrochim. Acta 52 (2006) 278.
[30] J.C. Ruiz-Morales, J. Canales-Vázquez, C. Savaniu, D. Marrero-López, W. Zhou, J.T.S. Irvine, Nature 439 (2006) 568.
[31] J. Høgh, K.V. Hansen, M. Mogensen, in: S. Linderoth, A. Smith, N. Bonanos, A. Hagen, L. Mikkelsen, K. Kammer, D. Lybye, P.V. Hendriksen, F.W. Poulsen, M. Mogensen, W.G. Wang (Eds.), Proceedings of the 26th Risø International Symposium on Materials Science: Solid State Electrochemistry, Risø National Laboratory, Roskilde, Denmark, 2005, pp. 235–240.

Please cite this article in press as: A. Tarancón, et al., J. Power Sources (2007), doi:10.1016/j.jpowsour.2007.08.077